Step-by-step from amorphous phosphate to nano-structured calcium hydroxyapatite: monitoring by solid-state 1 H and 31 P NMR and spin dynamics

Vytautas Klimavicius, Arūnas Maršalka, Agne Kizalaite, Aleksej Zarkov, Aivaras Kareiva, Kęstutis Aidas, Jérôme Hirschinger, Vytautas Balevicius

Step-by-step from amorphous phosphate to nano-structured calcium hydroxyapatite: monitoring by solid-state ^{1}H and ^{31}P NMR and spin dynamics

Vytautas Klimavicius[1], Arūnas Maršalka[1], Agne Kizalaite[2], Aleksej Zarkov[2], Aivaras Kareiva[2], Kęstutis Aidas[1], Jérôme Hirschinger[3], Vytautas Balevicius[1*]

[1]*Institute of Chemical Physics, Vilnius University, LT-10257 Vilnius, Lithuania*

[2]*Institute of Chemistry, Vilnius University, LT-03225 Vilnius, Lithuania*

[3]*Institut de Chimie, Université de Strasbourg, UMR 7177 CNRS, Strasbourg, France*

**Corresponding author, E-mail: vytautas.balevicius@ff.vu.lt*

Abstract

The solid-state ^{1}H, ^{31}P NMR spectra and cross-polarization (CP MAS) kinetics in the series of samples containing amorphous phosphate phase (AMP), composite of AMP + nano-structured calcium hydroxyapatite (nano-CaHA) and high-crystalline nano-CaHA were studied under moderate spinning rates (5-30 kHz). The combined analysis of the solid-state ^{1}H and ^{31}P NMR spectra provides the possibility to determine the hydration numbers of the components and the phase composition index. A broad set of spin dynamics models (isotropic/anisotropic, relaxing/non-relaxing, secular/semi-non-secular) were applied and fitted to the experimental CP MAS data. The anisotropic model with the angular averaging of dipolar coupling was applied for AMP and nano-CaHA for the first time. It was deduced that the spin diffusion in AMP is close to isotropic, whereas it is highly anisotropic in nano-

CaHA being close to the Ising-type. This can be caused by the different number of internuclear interactions that must be explicitly considered in the spin system for AMP (I–S spin pair) and nano-CaHA (I_N–S spin system with $N \geq 2$).

The P–H distance in nano-CaHA was found being significantly shorter than its crystallographic value. An underestimation can be caused by several factors, among those - proton conductivity via a large-amplitude motion of protons (O–H tumbling and the short-range diffusion) that occurs along OH^- chains. The P–H distance deduced for AMP, i.e. the compound with HPO_4^{2-} as the dominant structure, is fairly well matching to the crystallographic data. This means that the CP MAS kinetics is a capable technique getting a complementary information on the proton localization in H-bond and the proton transfer in the cases, where traditional structure determination methods fail.

1. Introduction

"Our populations are aging. Some experts predict that 30% of hospital beds will soon be occupied by osteoporosis patients" – this sentence was brought out beginning the review article by Bohner *et all*.[1] The bone tissue consists of about 70% of calcium phosphates (CaPs) that makes CaPs materials of choice for potential treating of bone diseases by repairing damaged bone tissues. Hydroxyapatites (HA) are thermodynamically the most stable form of CaPs, and therefore they are very attractive objects for investigation as from the physical point as well as for applications. The most important applications are: preparation of biocompatible materials such as artificial bones and teeth catalysis, pharmaceutics, fertilizers, protein chromatography etc.[2-4] Each particular application depends on HA structure, crystallinity, particles size, and morphology. This causes the growing interest to HA synthesis. Several synthesis routes, such as wet precipitations, sol-gel, reverse micelle templates, hydrothermal method, etc. have been developed and used.[4-6]

Calcium hydroxyapatite ($Ca_{10}(PO_4)_6(OH)_2$, CaHA) represents a privileged member for the applications due to its close resemblance to the mineral of hard tissues (bone, enamel, dentin, *etc.*) resulting in high biocompatibility.[2-4] The interest to CaHA arises from the physical point of view because it belongs to the class of low-dimensional proton-conducting materials possessing a large-amplitude motional freedom of protons along OH^- chains.[7,8] An interplay between the surface and bulk effects results in other interesting features of the nano-structured CaHA (nano-CaHA).[9] Nevertheless, the dynamic features and structural manifolds in CaHA are still not well understood.

The solid-state NMR is a proper tool for the studies of these problems. There was published a plenty of works on CaPs performed using NMR spectroscopy. The ^1H and ^{31}P chemical shifts were analyzed at the visual resolution or decomposing the complex signal shapes.[9-14] However, in many cases the peaks were assigned rather intuitively, without any adequate support from quantum

chemistry side. It has to be noted the work on octacalcium phosphate.[15] The high-level DFT calculations of ^{31}P magnetic shielding tensors were performed for the unit cell that consists of hydrated and apatitic layers. The ^{31}P chemical shifts were rigorously assigned basing on the calculation results.[15]

Another widely used NMR technique is the cross-polarization (CP), often combined with magic-angle spinning (MAS).[15-18] Typically, CP is used to enhance signals of less abundant spins (S) by using magnetization of abundant ones (I) with larger gyromagnetic ratio. CP is also feasible between abundant nuclei. Despite the signal enhancement in such case is ineffective, the CP technique between abundant nuclei is very useful extracting the unique information on the structure and dynamics of complex materials through the time (contact time) evolution of communication between the subsystems of interacting spins.[19] As CP is promoted by the dipolar I–S interactions that are intrinsically sensitive to internuclear distances, it plays a major role for probing short-range ordering and local dynamics.[20,21] This technique can reveal fine aspects of structural organization at the atomic level in soft and complex solids, where other traditional methods work unsatisfactorily.[22-24]

Traditionally, in the presence of strong heteronuclear dipolar coupling, the CP kinetics is described by the so-called I–I*–S model combining a coherent term of the isolated I*–S spin pair and an incoherent term related to interactions with other protons in a thermal spin-bath in a phenomenological way.[18,19,22] However, in the works on CaHA only the classical I–S and isotropic I–I*–S models were used.[10,11,23-26] There are no works, where the angular averaging of spin coupling, that is necessary for powder samples, was carried out.

In the present work, the series of the samples containing amorphous phosphate phase (AMP), composite of AMP + nano-structured calcium hydroxyapatite (nano-CaHA) and high-crystalline

nano-CaHA was synthesized and studied applying solid-state NMR techniques (^{1}H and ^{31}P NMR spectra as well as CP MAS kinetics). The comparative study monitoring the changes in NMR spectra along this series allows deeper to understand the stages of nano-structuring. The DFT calculations of the ^{1}H and ^{31}P magnetic shielding tensors of crystalline CaHA were performed for theoretical support to the peak assignments and for some supplementary insights into the experimental observations.

The earlier studies on CaHA have revealed that the nano-CaHA is a slowly relaxing spin system.[23,24] This makes the nano-CaHA very suitable for the testing of various microscopic quantum models of spin dynamics without taking into account the spin-lattice relaxation effects. A broad set of spin dynamics models (isotropic/anisotropic, relaxing/non-relaxing, secular/semi-non-secular) were applied and fitted to the experimental CP MAS data.

2. Experimental

Materials. Three different synthesis routes have been used that produced the samples containing amorphous phosphate phase (AMP), composite of AMP + nano-structured calcium hydroxyapatite (AMP+nano-CaHA) and high-crystalline nano-CaHA, respectively. More details of synthesis are given in the Electronic supplementary information (ESI). In order to remove the adsorbed water from nano-CaHA, the sample was vacuum-dried at 373 K for four days.

The characterization of the samples. The synthesis products were characterized by scanning electron microscopy (SEM) and energy-dispersive X-ray analysis (EDX) using a Helios NanoLab 650 scanning electron microscope coupled with energy-dispersive X-ray spectrometry system. SEM micrographs of CaHA samples prepared by Synthesis I - III are shown in Fig. 1.

X-ray diffraction (XRD) data were collected in the range of $10 \leq 2\theta \leq 60°$ using Ni-filtered CuK_α radiation on Rigaku MiniFlex II diffractometer working in Bragg-Brentano ($\theta/2\theta$) geometry. The XRD patterns of the samples are shown in Fig. 2. As it is seen, the XRD diffraction patterns contain diffraction lines attributable to calcium hydroxyapatite. The obtained results are in a good agreement with the reference data for $Ca_{10}(PO_4)_6(OH)_2$ (PDF [72–1243]).

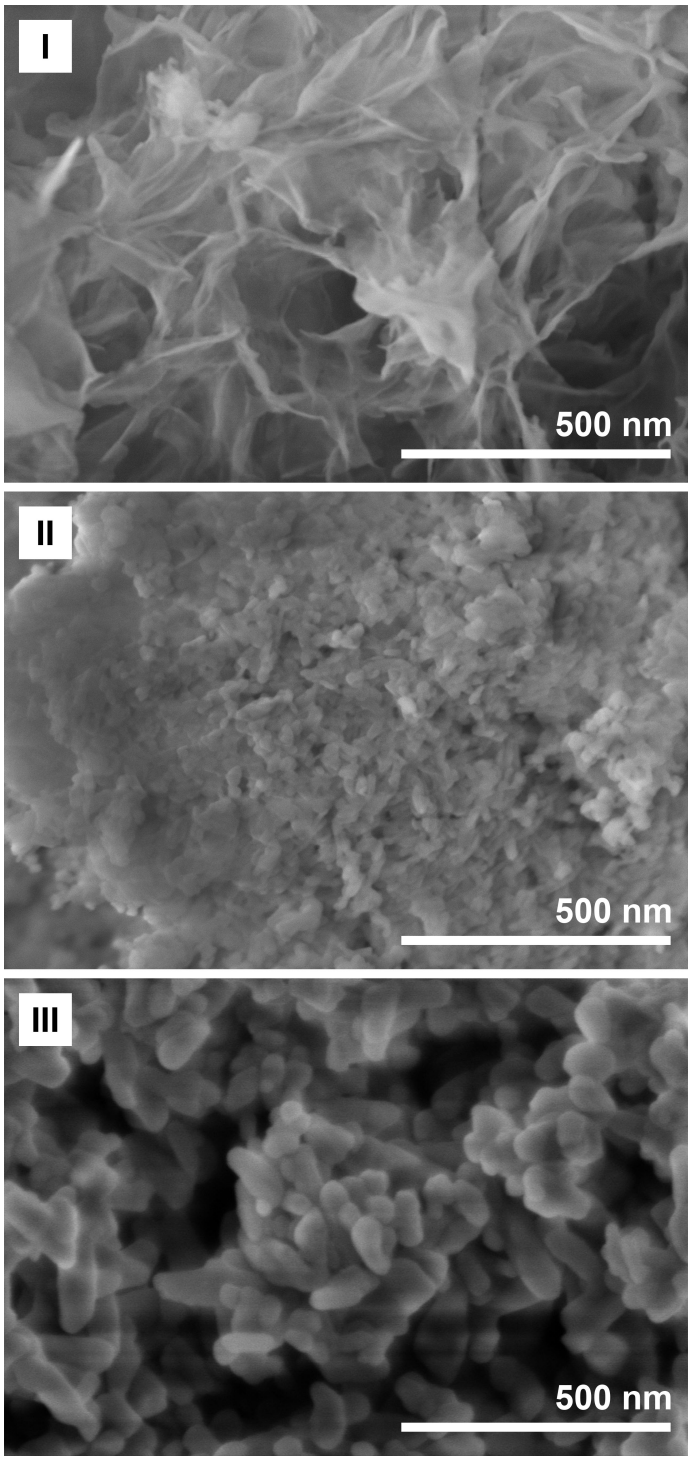

Fig. 1 SEM micrographs of the samples prepared by Synthesis I-III.

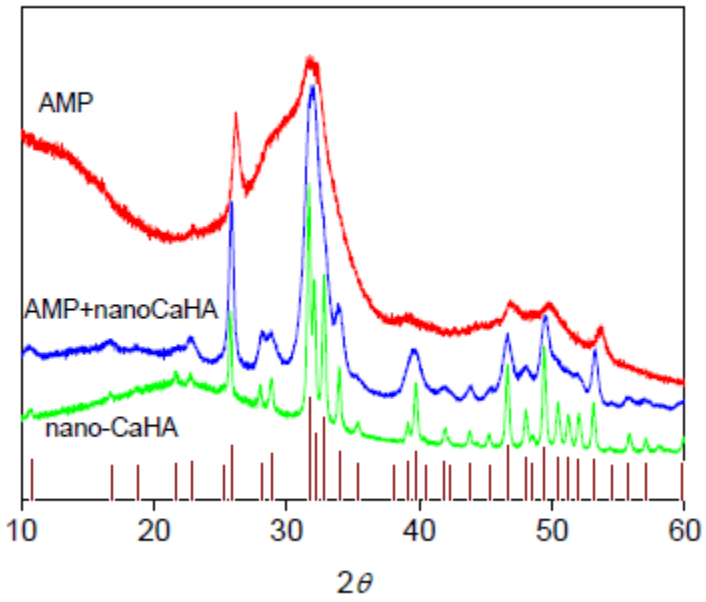

Fig. 2 XRD patterns of AMP, composite AMP + nano-CaHA and high-crystalline nano-CaHA samples.

***NMR measurements*.** The solid-state NMR experiments were performed using 600 MHz Bruker AVANCE NEO NMR spectrometer equipped with 2.5 mm Bruker TriGamma triple resonance MAS probe. The experiments were performed in 14.095 T magnetic field using Ascend 54 mm standard-bore superconducting magnet. The resonance frequencies of ^{1}H and ^{31}P nuclei were 600.3 MHz and 243.0 MHz, respectively. The $^{1}H \rightarrow ^{31}P$ CP MAS experiments were performed for the spinning sample at 5, 10, 20 and 30 kHz at the n = + 1 and + 2 Hartmann-Hahn (HH) matching condition. The CP contact was achieved with rectangular 71 kHz RF pulses for ^{31}P and properly varying it for ^{1}H (Fig. 3). The sample temperature was set to 298 K and controlled by Bruker BCU II temperature regulation system. The ^{1}H and ^{31}P chemical shifts were referenced to external standards of tetra-methylsilane (TMS) and 85% H_3PO_4 aqueous solution, using adamantane ($\delta(^{1}H)$ = 1.85 ppm) and ammonium dihydrogen phosphate ($\delta(^{31}P)$ = 0.8 ppm), respectively. Spectra

consisted of 7142 real data points and were registered using single scan, the repetition delay was set to 125 s which is equal to 5· T_1 (^{1}H). The CP MAS kinetics were registered by varying the contact times from 50 μs to 10 ms in increments of 10 μs. Processing of CP MAS kinetics was carried out using the Microcal Origin and MathCad packages.

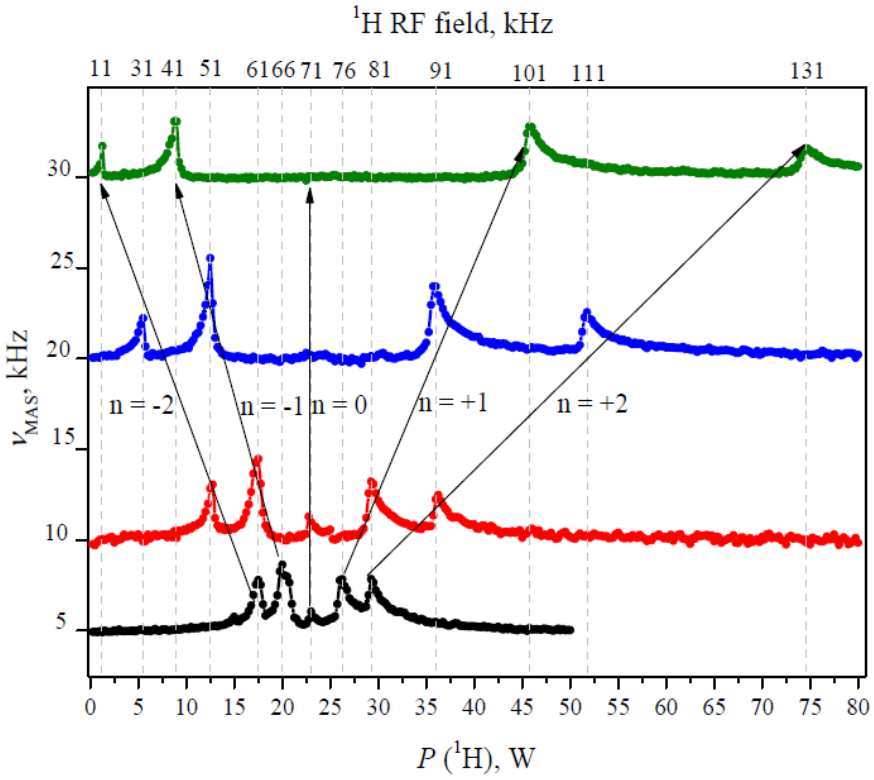

Fig. 3 Hartmann-Hahn (HH) matching profile in nano-CaHA (dry sample) at contact time t = 2 ms for various MAS rates.

3. DFT calculations

In order to evaluate the ^{1}H and ^{31}P isotropic shielding constants of hydroxyl groups in the channels as well as in the bulk and on the surface of calcium hydroxyapatite, two truncated

structural models were constructed based on the hexagonal $P6_3/m$ X-ray structure of calcium hydroxyapatite (CIF ID: 9011091).[27] A series of 6 consecutive hydroxyl groups is surrounded by the inner most phosphate moieties and calcium ions as depicted in Fig. 4. The atomic coordinates used in the calculation are given in ESI. In the two models, OH^- groups face up or down as seen in Figs 4a and 4b, respectively. The net charge of the calcium cations and phosphate anions is zero in both models, thus the total charge of the entire system of -6 is determined solely by the number of hydroxyl groups.

The NMR isotropic shielding constants have been computed using the PBE0 exchange correlation functional.[28] The two central OH^- groups as highlighted in Fig. 4 have been described by the 6-311++G(2d,2p) basis sets, while the smaller 6-31G* basis set was employed for the rest of the system. The electronic structure calculations have been performed by using the Gaussian16 suite of programs.[29] This approach was proven to be adequate in various cases earlier. For example, satisfactory agreement between calculated and experimentally measured NMR chemical shifts was obtained for molecular systems involved in strong H-bonding and also for rather 'inert' species, e.g. CH_3 protons.[30]

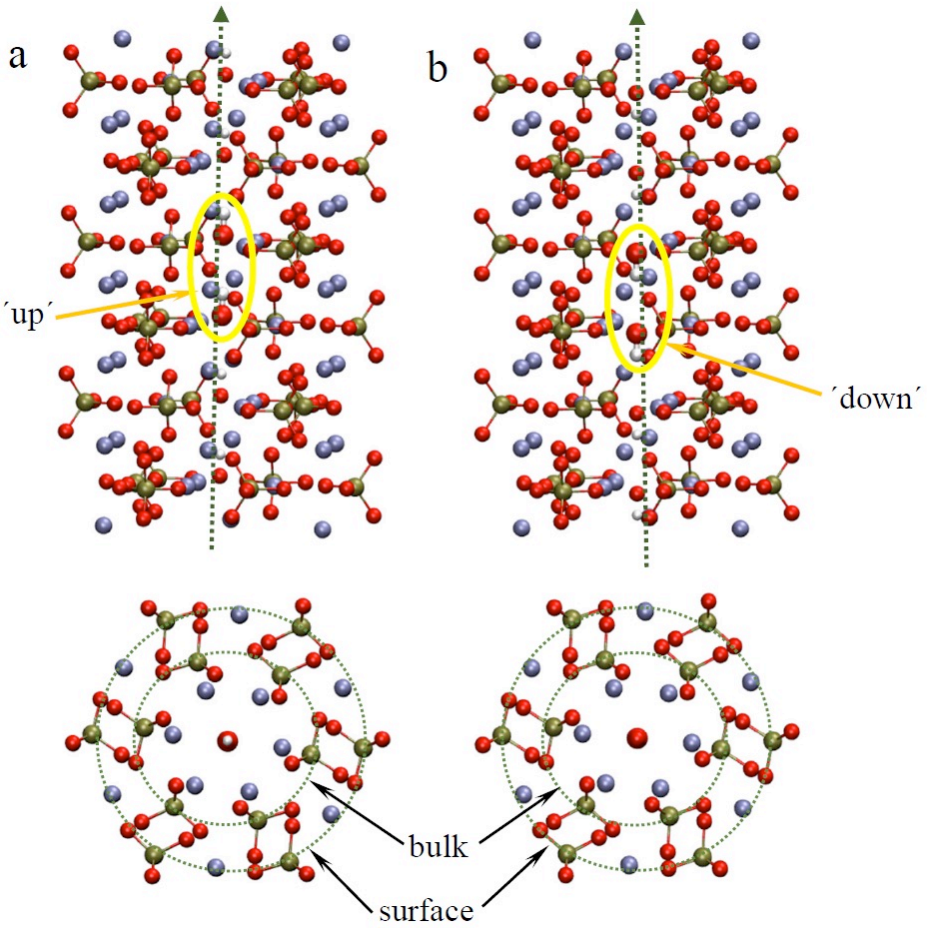

Fig. 4 Structural models of hexagonal CaHA with ´up´ (a) and ´down´ (b) configurations of hydroxyl groups. Top panel – side view, bottom panel – top view. Color code: red – oxygen atoms, white – hydrogen atoms, tan – phosphorus atoms, blue – calcium cations.

4. Theoretical spin dynamics models

Many of widely used theoretical CP kinetic models that exhibit the coherent oscillatory behavior of intensity originate from the pioneer work of Müller *et al*.[31] Later on, it was called as the I–I*–S model.[18,19,22] The spin system is treated as a strongly coupled I*–S spin pair immersed in a spin-bath consisting of the remaining I spins (I = ^{1}H and S = ^{31}P in the present work). There is assumed

that only one spin I^* interacts with the I-spin bath (or infinite energy reservoir of I spins), which is described in a phenomenological way.

The spin dynamics is described by the time evolution of the reduced density operator $\hat{\boldsymbol{\sigma}}(t)$ solving the generalized Liouville-von Neumann differential equation

$$\frac{d}{dt}\,\hat{\boldsymbol{\sigma}}(t) = -i\left[\widehat{\boldsymbol{H}_S}, \hat{\boldsymbol{\sigma}}(t)\right] - \hat{\hat{\boldsymbol{\Gamma}}}\left(\hat{\boldsymbol{\sigma}}(t) - \hat{\boldsymbol{\sigma}}(\infty)\right), \tag{1}$$

where $\widehat{\boldsymbol{H}_S}$ is the system Hamiltonian, and $\hat{\hat{\boldsymbol{\Gamma}}}$ is the spin-diffusion superoperator.[18,22,32] For a fast fluctuating I-spin bath, the spin diffusion superoperator can be written as[32]

$$\hat{\hat{\boldsymbol{\Gamma}}}(\hat{\boldsymbol{\sigma}}) = R^I_{dp}\left[\widehat{\boldsymbol{I}_z}, \left[\widehat{\boldsymbol{I}_z}, \hat{\boldsymbol{\sigma}}\right]\right] + R^I_{df}\left\{\left[\widehat{\boldsymbol{I}_x}, \left[\widehat{\boldsymbol{I}_x}, \hat{\boldsymbol{\sigma}}\right]\right] + \left[\widehat{\boldsymbol{I}_y}, \left[\widehat{\boldsymbol{I}_y}, \hat{\boldsymbol{\sigma}}\right]\right]\right\} + R^S_{df}\left\{\left[\widehat{\boldsymbol{S}_x}, \left[\widehat{\boldsymbol{S}_x}, \hat{\boldsymbol{\sigma}}\right]\right] + \left[\widehat{\boldsymbol{S}_y}, \left[\widehat{\boldsymbol{S}_y}, \hat{\boldsymbol{\sigma}}\right]\right]\right\}, \tag{2}$$

where R^I_{dp} and R^I_{df} are the (homonuclear) spin-diffusion rate constants of the I^* spin and R^S_{df} is that of the S spin (heteronuclear). The rate constants R^I_{df} and R^S_{df} are associated with the flip-flop terms of the homonuclear (I–I^*) and heteronuclear (I–S) dipolar Hamiltonians, respectively, and allow the complete thermal equilibration with the bath, whereas R^I_{dp} acts on the damping of the coherence driving the system to the internal quasi-equilibrium.[32]

The solution of the general non-secular equation is rather cumbersome to implement. A series of the simple analytical solutions were derived in the *secular* approximation, *i.e.*, under the conditions : i) the applied RF fields are much stronger than I^*–S coupling (ω_{1I}, $\omega_{1S} >> |b|$); ii) the I^*–S coupling constant is much larger than the spin diffusion rate constants ($|b| >> R^I_{df}, R^I_{dp}$). In ref

32 it was shown that the generalized Liouville-von Neumann equation has a *semi-non-secular* analytical solution under a softer condition $|b| >> |R^I_{df} - R^S_{df}|$. The approaches used in the present work are listed below.

The secular anisotropic non-relaxing model for* I*–S *spin pair (further – SEC). The CP kinetics, i.e. the dependence of the CP signal intensity $I(t)$ on the contact time t is written as[32]

$$I(t) = \langle\langle \hat{\sigma}(t)\widehat{S_z}\rangle\rangle = I_0\left[1 - \frac{1}{2}e^{-R^{\Sigma}_{df}t} - \frac{1}{2}e^{-\left(R^{\Sigma}_{df}+R^{I}_{dp}/2\right)t}\langle\cos(bt)\rangle_{AA}\right], \quad (3)$$

where the brackets $\langle\ldots\rangle_{AA}$ means the angular averaging, $R^{\Sigma}_{df} = R^I_{df} + R^S_{df}$ and R^I_{dp} are the spin-diffusion rates (Eq. (2)); the cosine-oscillation frequency b depends on the gyromagnetic ratios (γ_I, γ_S) of the two interacting nuclei (I and S), the distance r between them and the angle θ between the $\boldsymbol{r}$ vector and the magnetic field:

$$b = \frac{\mu_0}{4\pi}\frac{\gamma_I\gamma_S\hbar}{r^3}\frac{\left(3\cos^2\theta - 1\right)}{2}. \quad (4)$$

Note, in the case of the isotropic spin-diffusion ($R^I_{df} = R^I_{dp} = R$) the Eq. (3) converts to the well-known expression derived in the work of Müller *et al.*[31]

As the dipolar splitting b is an 'angular' function, the proper angular averaging has to be performed in order to adapt this equation to powder samples.[33,34] The angular averaging (AA) for CP MAS experiments is carried out as

$$\langle\cos(b\,t)\rangle_{AA} = \frac{1}{2}\int_0^{\pi}\cos(b(\beta)\,t)\sin(\beta)d\beta. \quad (5)$$

where β is the polar angle between $\boldsymbol{r}$ vector and the MAS rotor axis.[33] Depending on the HH matching condition $\omega_{1I} - \omega_{1S} = n\omega_{MAS}$ is fulfilled ($n = \pm 1, \pm 2$, the present work), the AA procedure has to be carried out on the cos($b_n t$) oscillation that contains the spherical components of the $\boldsymbol{b}$-tensor

$$b_{\pm 1} = \frac{D_{IS}}{2\sqrt{2}} \sin(2\beta), \; b_{\pm 2} = \frac{D_{IS}}{4} \sin^2\beta, \tag{6}$$

where D_{IS} is the heteronuclear I–S dipolar coupling constant $D_{IS} = (1/2\pi)\,(\mu_0/4\pi)\,\gamma_I\gamma_S\,(h/2\pi)/r^3$ (in Hz). The angular averaging was carried out numerically in all cases.

The anisotropic relaxing model (Naito and McDowell,[35] corrected by Hirschinger and Raya,[36] further – cNMD). The secular non-relaxing model (Eq. (3)) was extended by Naito and McDowell, taking into account the rates of spin-lattice relaxation processes in the rotating frame ($R^I_{1\rho} = 1/T^I_{1\rho}$, $R^S_{1\rho} = 1/T^S_{1\rho}$). The original Naito-McDowell equation[35] is for convenience rewritten in the notations of Eq. (2), replacing $R_I + R_S \rightarrow R^{\Sigma}_{df}$, $R^{\Sigma}_{1\rho} = R^I_{1\rho} + R^S_{1\rho}$ and $R^Z_I \rightarrow R^I_{dp}$ as

$$I(t) = I_0 \left\{ \left[\frac{1}{2} - \frac{R^{\Sigma}_{df}}{R^{\Sigma}_{df} + R^S_{1\rho}} \right] \mathrm{e}^{-\left(R^{\Sigma}_{df} + R^{\Sigma}_{1\rho}\right)t} + \left(\frac{R^{\Sigma}_{df}}{R^{\Sigma}_{df} + R^S_{1\rho}} \right) \mathrm{e}^{-R^I_{1\rho} t} - \right.$$

$$\left. \frac{1}{2} \mathrm{e}^{-\frac{1}{2}\left(R^I_{dp} + 2R^{\Sigma}_{df} - R^S_{1\rho} + R^I_{1\rho}\right)t} \cos(b\,t) \right\}. \tag{7}$$

As expected, Eq. (7) converts into Eq. (3) in the case of very slow spin-lattice relaxation in the rotating frame ($1/T^I_{1\rho} \rightarrow 0$, $1/T^S_{1\rho} \rightarrow 0$). However, we have recently shown that the solution

originally derived by Naito and McDowell (Eq. (7)) is *incorrect* in the presence of $T_{1\rho}$ relaxation.[36] The correct NMD (cNMD) solution with the angular averaging procedure is written[36]

$$I(t) = I_0 \left\{ \left[\frac{1}{2} - \frac{R^{\Sigma}_{df}}{R^{\Sigma}_{df} + R^{S}_{1\rho}/2 - R^{I}_{1\rho}/2} \right] \mathrm{e}^{-\left(R^{\Sigma}_{df} + R^{\Sigma}_{1\rho}/2\right)t} + \left(\frac{R^{\Sigma}_{df}}{R^{\Sigma}_{df} + R^{S}_{1\rho}/2 - R^{I}_{1\rho}/2} \right) \mathrm{e}^{-R^{I}_{1\rho} t} - \frac{1}{2} \mathrm{e}^{-\left(R^{\Sigma}_{df} + R^{I}_{dp}/2 + R^{\Sigma}_{1\rho}/4\right)t} \langle \cos(b\, t) \rangle_{AA} \right\}. \quad (8)$$

Note that the amplitudes of the two incoherent terms are corrected simply by replacing $R^{S}_{1\rho}$ by $R^{S}_{1\rho}/2 - R^{I}_{1\rho}/2$. The cNMD solution (Eq. (8)) not only exhibits the expected decaying rate ($R^{\Sigma}_{1\rho}/2$) in the limiting case of an Ising system–environment interaction ($R^{\Sigma}_{df} = 0$),[22] but also shows a reduced damping rate ($R^{\Sigma}_{1\rho}/4$) for the coherent term.

Secular anisotropic model for spin clusters $\mathbf{I}^{*}_{N}$**–S** (Kolodziejski and Klinowski,[19] further – SEC-C). Both above models (Eqs (3) and (8)) consider a I^{*}–S spin pair. It was be modified for the spin clusters I^{*}_{N}–S introducing the parameter λ that is related to the cluster size N.[19] In the case of very long relaxation $T^{S}_{1\rho} \to \infty$ (note, this is indeed true for nano-CaHA), it is written as

$$I(t) = I_0 e^{-t/T^{I}_{1\rho}} \left\{ 1 - \lambda \mathrm{e}^{-R^{\Sigma}_{df} t} - (1 - \lambda) \mathrm{e}^{-\left(R^{\Sigma}_{df} + R^{I}_{dp}/2\right)t} \langle \cos(b\, t) \rangle_{AA} \right\}. \quad (9)$$

As λ depends on the group mobility it must be adjusted by the fitting of experimental and calculated curves. Its value optimized for a I^{*}_{2}–S spin system is ~ 0.25 - 0.33.[19,37] In the limit $R^{I}_{dp} >> R^{I}_{df}$ (highly anisotropic case), it is possible to distinguish two regimes: one in which the I^{*}_{N}–S spin system decoheres and reaches a quasi-equilibrium state characterized by R^{I}_{dp} and the other in which polarization transfer from the bath is completed with a rate R^{Σ}_{df}. The parameter λ then

accounts for the fact that the quasi-equilibrium state polarization does not coincide with the time averaged value in an isolated I_N–S spin system.[18] This model (with some modifications, however, without AA) was most often used in the CP MAS studies of HAs and related systems.[10,23-26] The isotropic spin-diffusion approach ($R^I_{df} = R^I_{dp} = R = 1/T_{df}$, T_{df} is the proton spin-diffusion time constant) was set in all those cases.

Semi-non-secular model (Hirschinger and Raya,[32] further – SNS):

$$I(t) = I_0\left[1 - \frac{1}{2}\mathrm{e}^{-R^{\Sigma}_{df}t}\left\{1 + \mathrm{e}^{-\frac{1}{2}R^I_{dp}t}\left\langle\left[\cosh(\varphi t) + \frac{R^I_{dp}}{2\varphi}\sinh(\varphi t)\right]\right\rangle_{AA}\right\}\right], \qquad (10)$$

where $\varphi = \sqrt{\left(R^I_{dp}/2\right)^2 - b^2}$. It is easy to notice that the transient oscillations of CP intensity will appear when φ becomes imaginary, i.e. $b^2 > (R^I_{dp}/2)^2$. If $(R^I_{dp}/2)^2 > b^2$, oscillations convert to an overdamped regime. This approach in preferable if the physical legitimacy to use the Eqs (3), (8) and (9) for describing weakly interacting spins ($b \approx R^I_{dp}$) is in a certain doubt.

5. Results and discussion

The signal shape analysis of ^{1}H and ^{31}P NMR spectra. This procedure is the most suitable for the monitoring of structural changes in the studied series going from AMP to nano-CaHA. The shapes of ^{1}H and ^{31}P NMR signals were analyzed in many works on CaHAs on various levels.[9-14] Perhaps the most detailed consideration is given in ref 9. There was pictured a complete visual 'map' of structural manifolds. However, for the sake of clarity, the spectral components of the complex NMR shapes were represented only schematically, avoiding the question to resolve them possessing real experimental data arrays. In other words, the chances to deduce the true number of

overlapping peaks and their parameters (positions, widths, intensities) on the statistically reasoned level were not discussed.

In the present work a precise ^{1}H and ^{31}P NMR signal contours analysis was carried out approaching the shapes of 'elementary' bands by Voigt functions. The non-linear multiple peak fitting was performed gradually increasing the number of the overlapping bands and keeping a check on the statistical parameters (the correlation coefficient R^2 and the sum of weighted squares of deviations χ^2) as well as on the errors of the optimized parameters. The procedure used to stop when no improvement in R^2 and χ^2 was noticed and the standard errors started to diverge.

Hence, in the present work the positions, widths and relative intensities of the separated spectral components were determined and presented in a realistic manner (Fig. 5). The fitting results depend on the perfection of the real experiment caused by instrumental settings, stability, signal-to-noise ratio, etc. Therefore, it is not surprising that not all peaks predicted in ref 9 were resolved. The attribution of some ^{31}P NMR peaks used in ref 9 was slightly revised on the ground of DFT calculation results taken from ref 15. There was carried out a very thorough high-level calculation of ^{31}P chemical shifts of octacalcium phosphate (OCP). As AMP contains significant amount of structural water (Fig. 5), it should be satisfactorily mimicking by the hydrated layer of OCP, whereas the apatitic layer is similar to nano-CaHA. The calculated ^{31}P chemical shifts decrease as $\delta(PO_4^{3-}\text{surf}) > \delta(PO_4^{3-}\text{bulk}) > \delta(HPO_4^{2-})$. The same tendency follows from the DFT calculations carried out in the present using the truncated model (Fig. 4). The ^{31}P isotropic shielding constant averaged over the phosphorous atoms in the internal circle, denoted in Fig. 4 as the bulk, appeared to be by ~ 7 ppm larger than that in the external one, i.e. on the surface (382 ppm and 375 ppm, respectively). As the chemical shifts are obtained by subtracting the computed isotropic shielding constants from the corresponding reference shielding constants this means that

$\delta(PO_4^{3-}\text{surf}) > \delta(PO_4^{3-}\text{bulk})$. The simple *in vacuo* calculation of the isotropic ^{31}P shielding constants of PO_4^{3-} and HPO_4^{2-} moieties indicates that $\delta(PO_4^{3-})$ should be ca 11 ppm higher than $\delta(HPO_4^{2-})$ (see ESI). Therefore, the above rules for the chemical shifts were adopted assigning the resolved ^{31}P NMR peaks in the present work (Fig. 5).

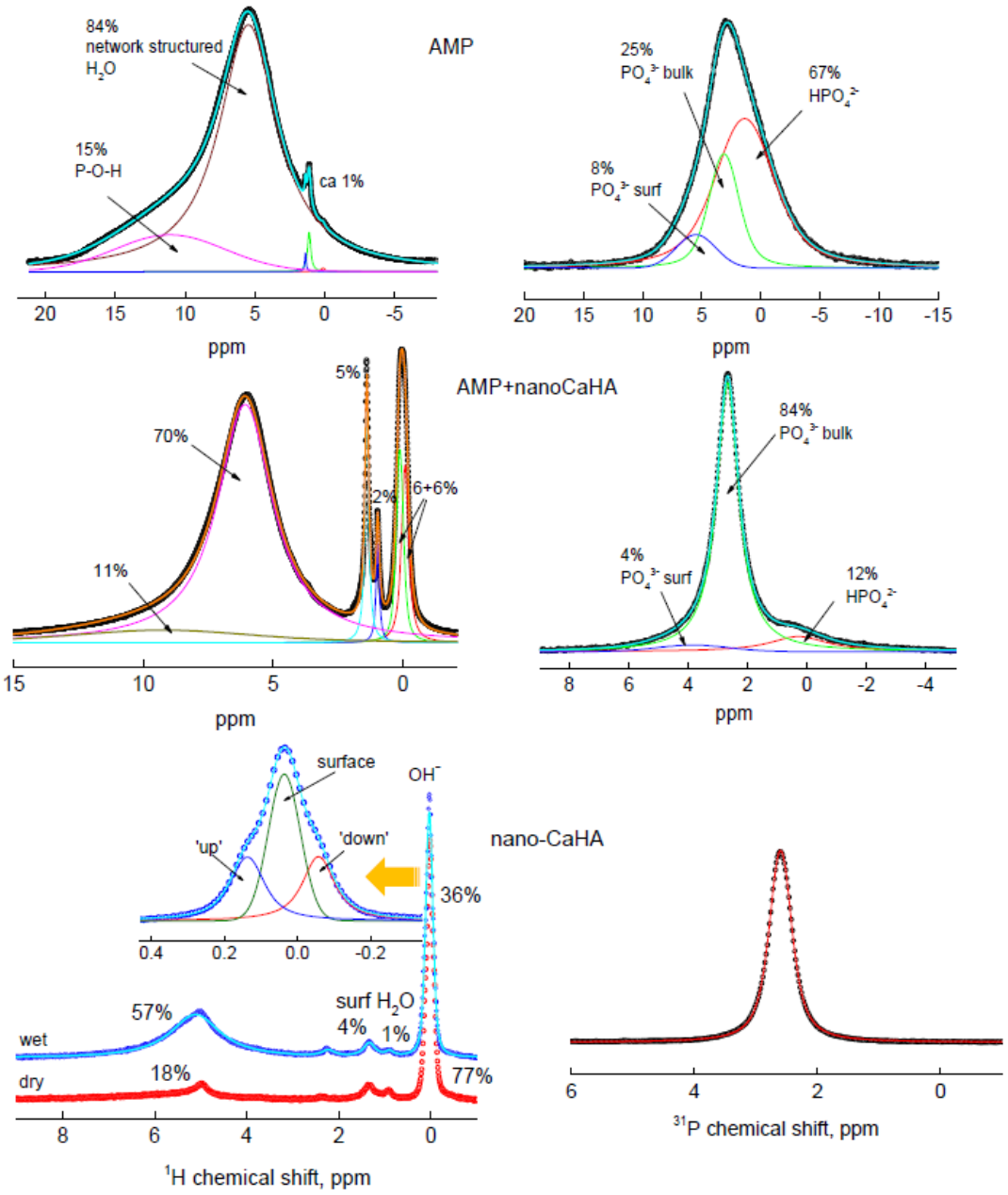

Fig. 5 The monitoring of structural changes in the studied series via the ^{1}H and ^{31}P NMR signal shape analysis (single pulse excitation, 10 kHz MAS). The positions of the decomposed spectral components and their relative integral intensities are represented in a realistic (percentage) manner. Denotations 'wet' and 'dry' mean the sample was prepared under ambient conditions and vacuum-dried (see ***Materials***).

As the integrated intensities of NMR signals are proportional to the numbers of corresponding nucleus, some quantitative evaluations of the structural contents can be done. The ^{1}H NMR signal at 5.5 ppm is clearly dominant in AMP (84%, Fig. 5). It is assigned to the structural water in the H-bond networks $(H_2O…H_2O…)_i$ with the aggregation number $i \geq 4$, i.e. water tetramers and higher.[38,39] The AMP sample is the most hydrated one in the studied series. Comparing the percentage of the integral intensities of P–O–H and HPO_4^{2-} peaks (Fig. 5) 0.15 N_H = 0.67 N_P, it follows $N_H/N_P = 4.5$ (within ± 10 % uncertainty). Then, the structure of AMP in the stoichiometric form is written as $Ca_3(PO_4)_2 \cdot (4.5 \pm 0.5)\ H_2O$.

Repeating this routine for P–O–^{1}H and H$^{31}PO_4^{2-}$ peaks in AMP + nano-CaHA sample, it follows that the hydration of AMP, being as one of the components of the composite, is strongly reduced to $N_P/N_H = 1.1 \pm 0.1$. A lower content of water in the composite sample can be due to the different synthesis route. However, it can be supposed that a significant amount of H_2O molecules moves to the sites on the crystallite surfaces of nano-CaHA. The drastic increase of intensities of the ^{1}H NMR peaks at 1.0 and 1.4 ppm (from less than 1% in AMP to 5% + 2% in the composite), i.e. the peaks attributed to water on the surfaces,[9,10,13] confirms this idea. Some amount of water molecules can occupy the isolated vacancies in OH^- chains.[14]

Roughly supposing that the HPO_4^{2-} may appear only as the defects to ideal CaHA structure,[9] the presence of these groups in nano-CaHA could be neglected. This indeed is supported by the ^{31}P NMR shape analysis. The single symmetrical peak centered at ~ 2.6 ppm was observed in nano-CaHA (Fig. 5). The peaks at this position are usually attributed to the PO_4^{3-} groups in the bulk.[9,10,12,13] Hence, there are no indications of the presence of the structural unit different from PO_4^{3-}. Such approach provides the possibility to characterize the phase purity of the composite by

properly defined phase composition indices. Possessing ^{1}H and ^{31}P NMR spectra and using integrated signal intensities, it can be done comparing the number of phosphorus atoms in coexisting phases. The integrals of OH^- and HPO_4^{2-} peaks in the ^{1}H NMR spectrum are almost equal (within ± 10 % uncertainty). As it is supposed that all protons in the nano-CaHA belong to the OH^- chains, the stoichiometric ratio N_P/N_H for $Ca_{10}(PO_4)_6(OH)_2$ is 3. The phase composition index can be defined via the atom numbers as $PC = (N_P/N_H)_{CaHA}/((N_P/N_H)_{CaHA} + (N_P/N_H)_{AMP})$. Hence, for the composite sample studied in the present work $PC = 0.75$.

Only two OH^- peaks centered at 0.13 ppm and – 0.08 ppm were resolved in the spectrum of the composite AMP + nano-CaHA (6% + 6%, Fig. 5). It was not succeeded to resolve three peaks as it was predicted in ref 9 and arbitrary assigned to ´up´ and ´down´ orientations of the hydroxyl groups in the OH^- columns and OH^- protons on the surfaces, respectively. However, it was succeeded in the nano-CaHA sample – three peaks in the approximate intensity ratio of 2:3:2 were resolved as in the 'wet' as well as in 'dry' samples (Fig. 5). This ratio was negligibly changing upon drying. It can be concluded that the drying of nano-CaHA removes only the H_2O molecules in the H-bond networks whereas its action on the structural water on the crystallite surfaces and on the OH^- chains is very weak. The DFT calculations show that the difference of the ^{1}H NMR isotropic shielding constants of the two central hydroxyl groups between the ´up´ and ´down´ structural configurations as shown in Fig. 4 is around 0.06 - 0.12 ppm. Having in mind the limitations of the truncated computational model applied in the present work, we find this result to lend reasonable support to the interpretation of experimentally observed difference of around 0.2 ppm of the two resolved peaks centered at around 0 ppm in the ^{1}H NMR spectrum shown in Fig. 5 to originate from the ´up´ and ´down´ configurations of the hydroxyl moieties.

The origin of the low-intensity peak at ~ 2.2 ppm in ^{1}H NMR spectrum of nano-CaHA is not clear. The change of its intensity under drying correlates with that of the structural water in H-bond network at ~ 5.5 ppm (Fig. 5). Probably, this peak belongs also to the H-bonded water, however, to the shorter aggregates (dimers or trimers)[37,38] captured in the vacancies of OH^- channels[14] or defects and cavities.

Spin dynamics. The ^{1}H – ^{31}P CP MAS kinetic experiments on AMP, the composite AMP + nano-CaHA and nano-CaHA were carried out at 20 kHz MAS and HH matching $n = +1$ (Fig. 6). In order to check the data reproducibility, two independent experiments were performed with AMP (run 1 and 2, Table 1). It is known that in AMP the processes of spin-lattice relaxation in the rotating frame occur in the time scale of ~ 10^{-2} s.[23,24] Therefore, the relaxing cNMD model (Eq. (8)) has be applied to describe the spin dynamics in AMP and for the amorphous component in composite AMP + nano-CaHA.

The non-linear curve fitting was carried out for all used models (Eqs (3), (8) - (10)) applying the Levenberg-Marquardt algorithm implemented in the Microcal Origin and MathCad packages. The quality of the fitting is demonstrated on the kinetic curves measured at 20 kHz MAS and HH matching for $n = +1$ (Fig. 6). The values of fitted parameters for all studied kinetics with statistical criterions are presented in Table 1.

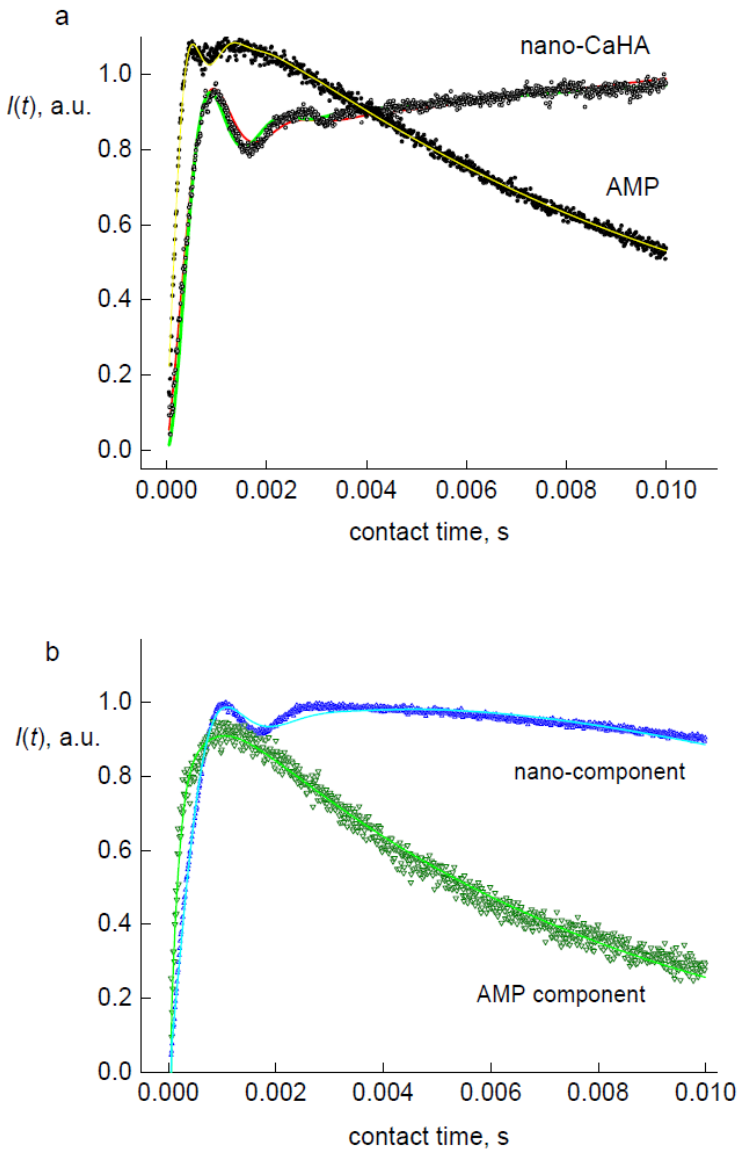

Fig. 6 Experimental $^{1}H - ^{31}P$ CP MAS kinetics (points): a) in AMP and nano-CaHA (dry sample) fitted using SEC (red line), SNS (green line) and cNMD (yellow line) models; b) in the composite AMP + nano-CaHA, both fitted by cNMD; all at 20 kHz MAS rate, HH matching n = +1, normalized and shifted along the ordinate axis for convenience. The values of fitted parameter are given in Table 1.

Table 1. The fitted model parameters for AMP, composite AMP+nano-CaHA and nano-CaHA.

Model	R^{Σ}_{df}, s^{-1}	R^{I}_{dp}, s^{-1}	$T^{I}_{1\rho}$, s	$T^{S}_{1\rho}$, s	*b*, Hz (no AA)	D_{IS}, Hz (with AA)	R^2/χ^2(%)
AMP, 20 kHz MAS, $n = +1$, cNMD model (Eq. (8))							
run 1	1170	2030	0.0096	0.0033	-	3290	0.997/1.4
run 2	1210	2020	0.0093	0.0051	-	3400	0.996/1.6
Composite AMP+nano-CaHA, 20 kHz MAS, $n = +1$							
amorphous component, cNMD (Eq. (8))	2110	8220*	0.0075	∞	-	2700	0.993/2.4
nano-CaHA component, SEC-C (Eq. (9)), $\lambda = 0.30$	810	960	0.06	∞	-	1160**	0.998/0.8
Nano-CaHA, SEC (Eq. (3)), SEC-C (Eq. (9)) and SNS (Eq. (10)) models							
5 kHz MAS, $n = +1$							
SEC	18	2030	∞	∞	1140	1570	0.988/1.8
SEC-C, $\lambda = 0.25$	70	1740	∞	∞	1190	1580	0.987/1.9
SNS	7	2030	∞	∞	1605	1770	0.986/2.0
10 kHz MAS, $n = +1$							
SEC	7	2220	∞	∞	1130	1550	0.965/2.8
SEC-C, $\lambda = 0.10$	380	1160	∞	∞	1230	1520	0.967/2.7
SNS	0	2300	∞	∞	1570	1790	0.967/2.8
10 kHz MAS, $n = +2$							
SEC	20	1980	∞	∞	850	1230	0.990/2.0

SEC-C, λ = 0.23	90	1790	∞	∞	920	1240	0.990/2.0
SNS	2	2190	∞	∞	1480	1620	0.985/3.1
20 kHz MAS, n = + 1							
SEC	23	2250	∞	∞	810	1190	0.991/1.7
SEC-C, λ = 0.22	260	1340	∞	∞	960	1210	0.995/1.3
SNS	7	2450	∞	∞	1340	1460	0.993/1.9

*- concerning this artifact, see comment in text; **- all b and D_{IS} values for nano-CaHA, which belongs to I_2–S spin system, are rescaled by $\sqrt{2}$, see explanation in text.

To our knowledge, in all works on CaHA and related systems, simplifying the CP MAS kinetics models, the approach $T^I_{1\rho} << T^S_{1\rho}$, $T^S_{1\rho} \to \infty$ was used. In the present work the cNMD model was applied, which includes the complete scheme of the rotating frame spin-lattice relaxation pathways. It was deduced that the processes of spin-lattice relaxation in the rotating frame in AMP occur in the same time scale of tens of milliseconds as for ^{1}H (= I) as well as for ^{31}P (= S) spins. However, a certain doubt arises concerning this result. Indeed, the determined relaxation rate of the S spin is much lower than the spin diffusion rate R^{Σ}_{df}, so that the precision of $T^S_{1\rho}$ must be very bad since only the sum of R^{Σ}_{df} and $1/T^S_{1\rho}$ appears in Eq. (8). This is not the case for the relaxation time of protons $T^I_{1\rho}$, because it solely drives the decay of the magnetization through the second exponential term of Eq. (8). The slowdown of the relaxation of ^{31}P spins ($T^S_{1\rho} \to \infty$) is seen in the composite sample and nano-CaHA (Table 1). Such behavior of spin-lattice relaxation times in the rotating frame ($T^I_{1\rho}$ and $T^S_{1\rho}$) is very similar to that observed in some polymers[40] – the higher content of structured water (Fig. 5), i.e. the larger proton bath, the faster relaxation (Table 1).

As it follows from the above signal shape analysis, the dominant structural unit in AMP is HPO_4^{2-} (67 %, Fig. 5). The spin system can be considered as a single S–I* spin pair ($^{31}P–O–^{1}H$) characterized by the heteronuclear dipolar coupling constant D_{IS} = 3350 ± 50 Hz. The cNMD model is valid for arbitrary values of the spin-diffusion and the relaxation rates as long as these rates are much lower than the S–I* dipolar coupling constant. The b value (in s^{-1}) ~ $2\pi D_{IS}$ fulfills this condition. Hence, the use of cNMD model is legitimated. The close values of R^I_{dp} and R^Σ_{df} deduced for AMP (R^I_{dp}/R^Σ_{df} ~ 2, Table 1) show the spin-diffusion in this system is close to isotropic. Note, the value R^I_{dp} ~ 8000 s^{-1} deduced for amorphous component in the composite sample seems to be a computational artifact - despite a good general fit, it was not succeeded to reproduce the first 'shake' of $I(t)$ at ~ 0.5 ms (green points and green line, Fig. 6b). This was because of low peak intensity (12 % of total, Fig. 5) and high noise level.

The heteronuclear dipolar coupling constant deduced for AMP corresponds to the P–H distance 2.44 ± 0.01 Å. This is a reasonable value for HPO_4^{2-}, knowing from crystallography[7,8,27] that the P–O and O–H distances in CaHA are 1.4 - 1.6 Å and ~ 0.94 Å, respectively. Hence, the experimental CP MAS kinetics and the applied spin-diffusion model correctly reproduce the P–H distance.

As distinct from AMP, the CP MAS kinetics in nano-CaHA measured at 5 kHz MAS rate pointed towards an extremely high anisotropy of spin-diffusion process in this system.[41] It even looks that the Ising-type interaction ($R^I_{df} = R^S_{df} = 0$) should be dominant. However, from the practice, the CP MAS experiments with HH sideband matching are rather sensitive to radiofrequency (RF) field inhomogeneity.[21,42-44] This impedes the interpretation of the spin diffusion rates or even leads to unreliable values. The extent of possible errors can be evaluated varying RF power, MAS rate and carefully matching the HH conditions. Therefore, in the present work the CP kinetics in nano-

CaHA have been studied (Fig. 7a) precisely matching HH conditions $n = \pm 1, \pm 2$ and varying the RF power within 76 - 131 kHz and the MAS rate from 5 to 30 kHz (Fig. 3). Note, some points on the kinetic curve measured at 30 kHz MAS were significantly dropped out. This could be due to the problem of the long-term spinning stability as this MAS rate was close to the technical limit of the probe. Therefore, despite the Fourier transform over the CP kinetics at 30 kHz provides rather conscious value of dipolar splitting (Fig. 7b), this curve was excluded from the further treatment. It is gratifying to see (Fig. 7b) that the experimental b values for $n = +1$ and $n = +2$ HH matching differ by the factor of $\sqrt{2}$, as it has to follow from the b_n definitions (Eq. (6)).

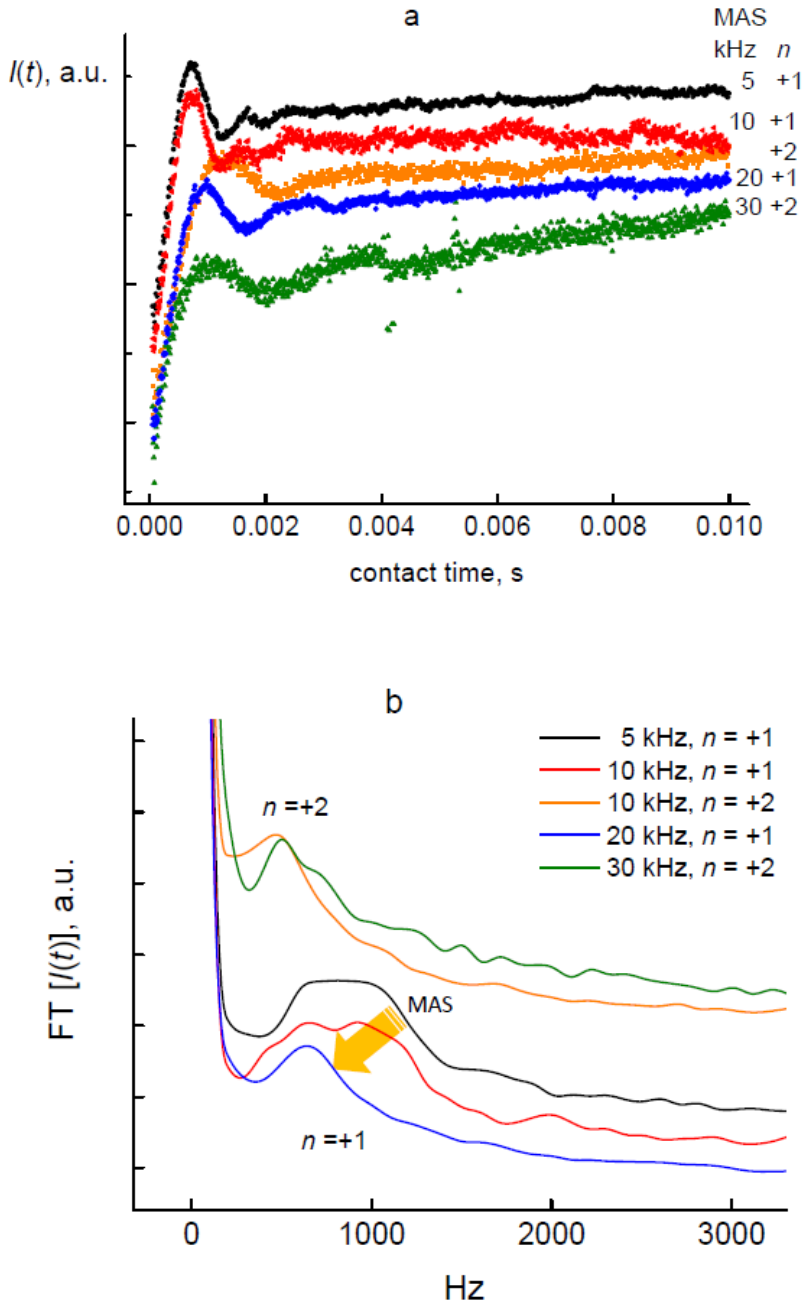

Fig. 7 (a) Experimental $^{1}H \rightarrow {}^{31}P$ CP MAS kinetics in nano-CaHA at various MAS rates and HH matching ($n = +1$ and $+2$); (b) Fourier transform over the corresponding CP intensities. The curves are shifted along the ordinate axis for convenience.

As nano-CaHA is a slowly relaxing spin system, i.e. $T^{I}_{1\rho}, T^{S}_{1\rho} \rightarrow \infty$,[23,24] the experimental curves (Fig. 7a) were fitted using non-relaxing SEC (Eq. (3)), SEC-C (Eq. (9)) and SNS (Eq. (10)) models, with- and without numerical angular averaging. The determined values of spin-diffusion rates, dipolar splitting and coupling constant are spread over a certain area, depending on the experimental settings (MAS rate and HH conditions) and the model was used (Table 1). The angular averaging effect is clearly seen in the D_{IS} *vs*. b plot using the b values that follow from the calculations with no AA (Fig. 8a). Depending on model, the AA procedure leads to the rescaling $D_{IS} \approx (1.2 \pm 0.1)b$.

It can be reasonably assumed that the calculations implementing the angular averaging (Eq. (5)) should provide more accurate evaluation of the spin-diffusion rates R^{I}_{dp} and R^{Σ}_{df}. For a powder, the destructive interference of the orientation-dependent coherences is expected to contribute significantly to the decay of the transient oscillations. The effect of the angular averaging is clearly seen on the R^{I}_{dp} values (with- and without AA, Fig. 8b), whereas it was not significant on the R^{Σ}_{df} values. Extremely low values of R^{Σ}_{df} indicate that the Ising-type interaction ($R^{I}_{df} = R^{S}_{df} = 0$) is indeed dominant in the nano-CaHA spin system. The calculations applying SEC-C model, i.e. including the I^{*}_{N}–S clusters, lead to slightly larger values $R^{\Sigma}_{df} \sim 10^{2}$ s^{-1} (Table 1, not shown in Fig. 8b). However, the anisotropy of spin-diffusion persists to be very high ($R^{I}_{dp}/R^{\Sigma}_{df} >> 1$). As the spin-diffusion in AMP is very close to isotropic, it can be supposed that the anisotropy of spin-diffusion is tightly coupled with the degree of anisotropy of proton baths. The proton bath in AMP consists of H-bonded water molecules in a bulky three-dimensional network (84 % of total water content), whereas in nano-CaHA it is formed of low-dimensional OH^{-} chains (77 %, Fig. 5). Alternatively, a slow fluctuation regime of the local fields controlled by the spin dynamics of the bath could explain the anisotropy of spin diffusion in nano-CaHA.[45]

Three kinetic models that were applied for nano-CaHA provide comparable values of statistical fit parameters (R^2/χ^2) as well as the strength of dipolar coupling (b, D_{IS}, Table 1). The knowing of the accurate D_{IS} values are important for the determination of ^{1}H–^{31}P distances.[42] The deduced D_{IS} values are dispersed over the range of ~ 1200 - 1800 Hz (Fig. 8a). According crystallography,[7,8,26] the shortest distance between ^{1}H and ^{31}P spins in CaHA is 3.847 Å that corresponds to $D_{IS} \approx 855$ Hz. The reasons of such discrepancy has to be discussed in more details.

The first point is the secularity. As the secularity condition $|b| >> R^I_{df}$, R^I_{dp} is not rigorously fulfilled, it can be suspected that the overestimation of D_{IS} is due to the illegal use of the secular models (SEC, SEC-C). The use of SNS model, which has much softer condition ($|b| >> |R^I_{df} - R^S_{df}|$), is then legitimate. However, the SNS model provides even higher D_{IS} values than the secular ones (Fig. 8a). Actually, the fact that the coupling constant fitted with the SNS solution is higher than the one obtained with the secular solution is expected due to the decrease of the transient oscillation frequency induced by the I–I* Ising term in the SNS model when b becomes comparable to R^I_{dp}. Furthermore, we have already noticed that this decrease is overestimated by the I–I*–S model (*cf.* Fig. 1a of ref 32).

The next factor for overestimation may arise because the nano-CaHA should be considered as a multiple-spin system. The crystallography data[26] show that there are in the OH^- chains two protons distanced from phosphorus by 3.85 Å. It is known that for multiple-spin systems the effective dipolar coupling b_{eff}, which value is determined from the CP oscillation frequency, has to be properly rescaled.[17,44] At 20 kHz MAS the SEC and SER-C models with the rescaling by a factor of $\sqrt{2}$ (i. e. considering that interactions other than the first two proton neighbors are neglected and the splitting of a perfect equidistant I_2–S CP spectrum at straight I–S–I angle, 180° or 0°) give the D_{IS} value ~ 1200 Hz (Table 1, Fig. 8a). This value is reasonably close to the expected one (855

Hz). However, assuming that the $n = \pm 1$ HH condition is *perfectly* matched, the CP spectra calculated for I_2–S systems with equal I–S internuclear distances are generally complex and exhibit four intense singularities and steep jumps whose positions largely depend on the angle χ between the two I–S vectors.[44,46,47] It has nevertheless been noticed that the I–S interatomic distance can be directly obtained from the χ-independent sub-splitting of the internal singularities, $S_{\mathrm{int}} = S_{\pm 1} = D_{IS}/\sqrt{2}$, for angles χ ranging from 45° to 135°.[44,46,47] This spin-pair-like splitting has been observed for strongly coupled CH_2 groups ($D_{IS} \approx 23$ kHz and $\chi \approx 109°$) in Lee-Goldburg CP MAS[46] and CP with varying contact time (CPVC) experiments under ultra-fast MAS.[48] These characteristic features are *not* detected experimentally in the case of the weak dipolar couplings ($D_{IS} \approx 1$ kHz) of nano-CaHA (Fig. 7b).

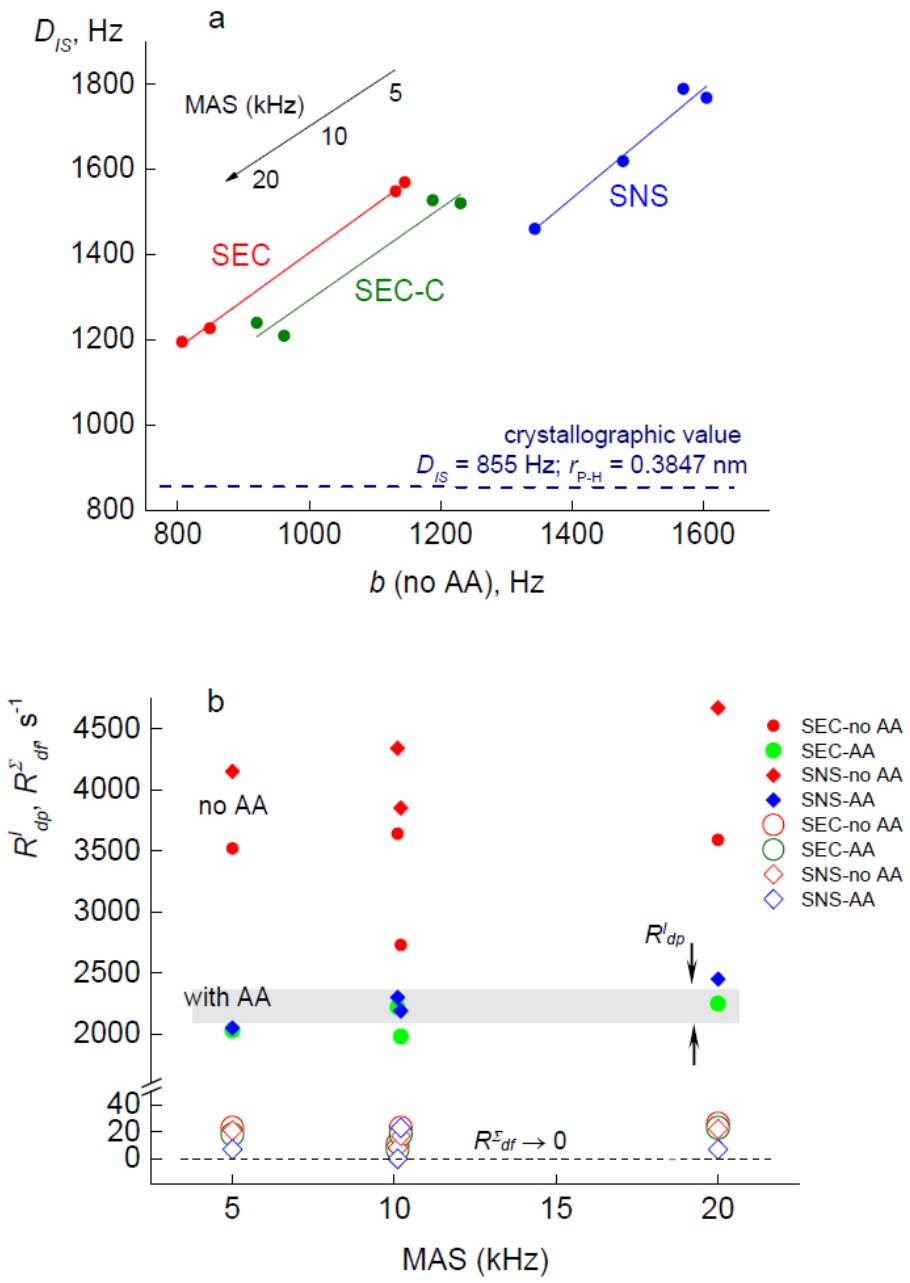

Fig. 8 The fitting results for nano-CaHA: (a) the D_{IS} *vs*. *b* plot, the *b* values were deduced from the model calculations without AA (Table 1); (b) the dependencies of spin-diffusion rates R^{I}_{dp} (filed symbols) and R^{Σ}_{df} (open symbols) at various MAS rates. More comments in text.

The third point is radiofrequency (RF) field mismatch/inhomogeneity. In principle, the CP MAS experiment with sideband HH matching is more sensitive to RF inhomogeneities than an experiment with matching at the static HH condition. Indeed, for sideband matching, the modified HH condition can no longer be fulfilled independently of the position of the spins within the sample volume.[49,50] RF inhomogeneity effects on HHCP are then expected to be important. However, a number of authors have successfully used CPVC to measure heteronuclear couplings and hence internuclear distances.[21,33,42,44,47,48,51] Actually, the practical robustness of CPVC has been attributed to the high spatial selectivity of the sideband HH matching conditions under fast MAS that overcomes complications caused by RF inhomogeneity[21,42,47] and to the truncation of the weak heteronuclear dipolar couplings by the much larger interaction of the strongly coupled spin pairs.[44] Although RF field inhomogeneity causes distortions and a decrease of the CP transfer efficiency the relevant splitting ($S_{\pm 1} = D_{IS}/\sqrt{2}$) of the Pake-like powder pattern obtained by Fourier transformation of the oscillatory CPVC kinetics is found to be little sensitive to experimental missettings.[21,42,47] However, it is noteworthy that this analysis is entirely based upon the simplified angular dependence of the polarization transfer for an isolated spin pair (γ encoding).[44] To the best of our knowledge, RF inhomogeneity effects have not been previously considered in the more complicated case of multiple-spin systems such as I_2–S and I_3 –S groups.[42,44,46,47] Indeed, the I_2–S CPVC spectrum leads to a γ-encoded powder pattern of splitting $S_{\pm 1}\sqrt{2} = D_{IS}$ *only* in the specific case of a straight angle ($\chi = 180°$ or 0°).[46]

In principle, a quantitative analysis of the effects of RF inhomogeneity would necessitate the knowledge of the RF field amplitudes at an arbitrary position within the sample volume. In the absence of such a detailed information and since the CP process in the high-field approximation only depends on the mismatch parameter $\Delta = \omega_{1I} - \omega_{1S}$ the main characteristics of the signal

may, nevertheless, be examined by assuming a given HH mismatch distribution $P(\Delta)$. A convenient choice for $P(\Delta)$ is the Gaussian distribution defined by

$$P(\Delta) = \frac{1}{\sigma_\Delta\sqrt{2\pi}} \exp\left[\frac{-(\Delta-\overline{\Delta})^2}{2\sigma_\Delta^2}\right] , \qquad (11)$$

where $\overline{\Delta}$ and σ_Δ are, respectively, the mean value and standard deviation of $P(\Delta)$. We have previously used this HH mismatch distribution to account for the effect of RF inhomogeneity on CPVC experiments and verified that only the general shape of $P(\Delta)$ is relevant.[21] It must also be pointed out that Eq. (11) gives CPVC lineshape distortions (*cf.* Fig. 6 of ref 21) that are very similar to the ones obtained by using a realistic model of the RF inhomogeneity profile across the sample space for single-coil probes.[42] The simulation of CPVC spectra (and CP kinetics) were performed using FORTRAN programs written by us. All other interactions, except the applied RF fields and the I–S or I_2–S heteronuclear dipolar coupling(s), were removed from the system Hamiltonian $\widehat{\boldsymbol{H}_S}$. $\widehat{\boldsymbol{H}_S}$ is then diagonalized analytically applying zeroth-order average Hamiltonian theory, as described previously.[21,44] The influence of the mismatch distribution $P(\Delta)$ on I–S and I_2–S CPVC spectra is reported in Fig. 9. In accordance with previous works,[21,42,47] the splitting of the I–S pair pake-like doublet is *independent* of the width of the RF field distribution and the effect of $P(\Delta)$ is limited to a slight loss of central intensity and a moderate inhomogeneous line broadening, in addition to the expected decrease in total signal amplitude (Fig. 9a). By contrast, it is readily seen that the CPVC spectra of I_2–S three-spin systems with I–S–I angles $\chi = 71°$ or 109° and $\chi = 30°$ or 150° are strongly affected by RF field inhomogeneity, the relevant internal singularities being barely visible as soon as σ_Δ/D_{IS} is higher than $\sim 1/4$ (Fig. 9b,c). This means that the observation of well resolved internal maxima is generally limited to coupling constants for which $\sigma_\Delta/D_{IS} \ll$

1, *i.e.*, $D_{IS}/2\pi \gtrsim 10$ kHz.[46,48] On the other hand, ccomplications caused by RF inhomogeneity must clearly be taken into account in the case of weakly coupled multiple-spin systems ($D_{IS}/2\pi \lesssim 1$ kHz). Fortunately, Fig. 9b,c shows that external singularities of splitting close to D_{IS} become prominent when $\sigma_\Delta/D_{IS} \gtrsim 1/4$. Furthermore, we have checked that a similar behavior is observed regardless of the angle χ. Assuming that the local spin geometry is a I_2–S system with equal I–S interatomic distances, this means that a simplified analysis of the CPVC spectra based on the isolated-like spin-pair approach can be used to get an estimation of the coupling constant D_{IS} provided that the scaling factor of $\sqrt{2}$ is taken into account. This is illustrated in Fig. 10, where the CPVC kinetics of the I_2–S triplet with $\sigma_\Delta/D_{IS} = 0.42$ is compared with that of an isolated I–S pair under perfect homogeneous HH matching. Indeed, the relevant first transient oscillation observed experimentally (Fig. 7a) is well reproduced by the I–S spin-pair calculation with $D_{IS}^{eff} = D_{IS}\sqrt{2}$. This allows an estimation of the coupling constant D_{IS} assuming the local geometries shown in Fig. 11 (I–S pair for AMP and I_2–S triplet for nano-CaHA).

It is pronounced in the experimental CP spectra obtained by Fourier transform over the CP MAS intensities (Fig. 7b). It should be noted that the determination of D_{IS} is more accurate using higher MAS rates,[21,47,48] because MAS averages out the proton homonuclear couplings. Indeed, the curve fitting at the MAS rates of ~ 20 kHz, applying SEC and SEC-C model provide the D_{IS} value that is the closest to the crystallographic one (855 Hz, $r_{P–H}$ = 3.847 Å, Figs 8a and 11). The remaining discrepancy may be attributed to a slight departure from the n = +1 HH matching condition[21,42,47] and/or to the fact that only the first two proton neighbors have been explicitely considered (I_2–S spin system) in Fig. 9b,c. Moreover, the fact that the transient oscillations of the CP MAS kinetics are strongly damped in multiple-spin systems (Figure 10 for $\chi \neq 0$ or 180°) may be accounted for by an increase of the Ising system-environment interaction rate constant R_{dp}^I in

the corresponding I–S spin-pair calculation. The observed highly anisotropic behavior ($R^I_{dp}/R^\Sigma_{df} \gg 1$) could then be attributed to the fact that the actual system size is larger than a I–S spin pair. Indeed, the inadequacy of the I–I*–S model to describe CP experiments in nano-CaHA is supported by several observations. First, all models reported in Section 4 assume that the spin population ratio N_{I*}/N_I is negligible (infinite reservoir of I spins). Whereas the high content of structured water can represent a proton bath in AMP ($N_{I*}/N_I = 0.15$), this is clearly not the case for nano-CaHA, especially for the 'dry' sample ($N_{I*}/N_I = 0.77$) (Fig. 5). Second, the SEC and SEC-C model provide a better agreement with the crystallographic data than the SNS model although the secular approximation breaks down. Third, the fitted values of the parameter λ in the SEC-C model (Table 1) indicate the presence of a I_N–S spin system with $N \geq 2$.[19] Fourth, both R^I_{dp} and R^Σ_{df} are found to be independent of the MAS rate (Table 1 and Fig. 8b) in contradiction with the fact that spin diffusion is expected to slowed down by MAS.

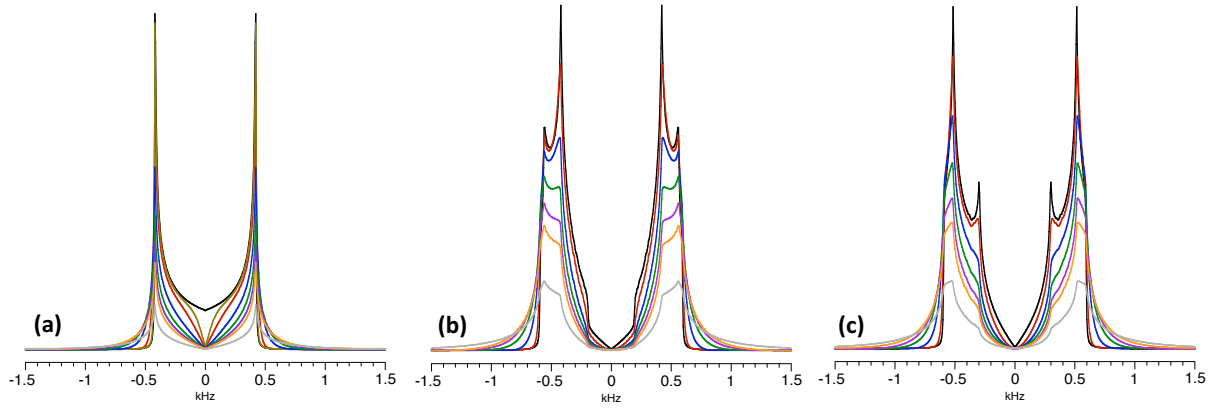

Fig. 9 Theoretical calculations of CPVC spectra in the case of (a) an isolated I–S spin pair (D_{IS} = 1188 Hz) and a I_2–S three-spin system ($D_{IS}^{(1)} = D_{IS}^{(2)} = 1188$ Hz) with an angle between the two I–S vectors (b) $\chi = 71°$ or 109° and (c) $\chi = 30°$ or 150° for $\overline{\Delta} = \pm\,\omega_r$ and several values of σ_Δ : $\sigma_\Delta = 0$ (black line), $\sigma_\Delta = 50$ Hz (brown line), $\sigma_\Delta = 0.1$ kHz (red line), $\sigma_\Delta = 0.2$ kHz (blue line), $\sigma_\Delta = 0.3$ kHz (green line), $\sigma_\Delta = 0.4$ kHz (purple line), $\sigma_\Delta = 0.5$ kHz (orange line), $\sigma_\Delta = 1$ kHz (grey line). The spectra are plotted on the same amplitude scale so that they can be directly compared.

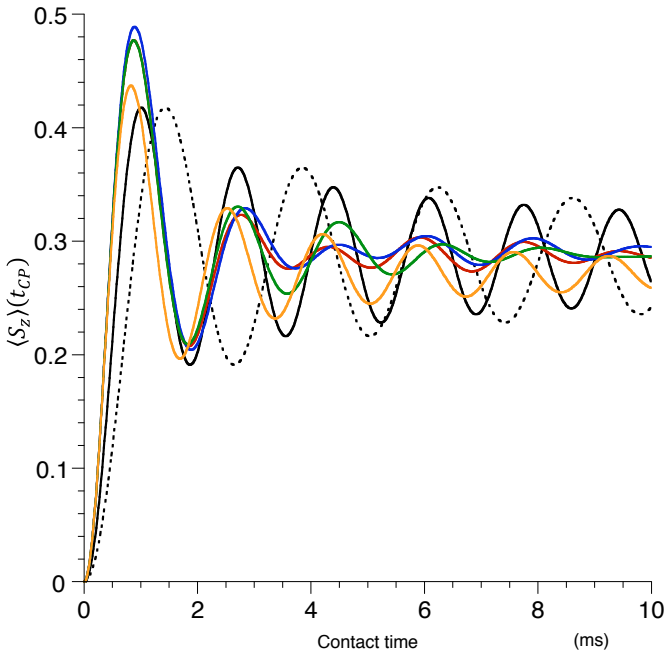

Fig. 10 Polarization evolution of the S-spin magnetization as a function of the CP contact time for an isolated I–S spin pair under perfect homogeneous HH matching with $\Delta = \pm\,\omega_r$ and $D_{IS} = 1680$ Hz (black solid line), $D_{IS} = 1188$ Hz (black dotted line) and for a I_2–S three-spin system ($D_{IS}^{(1)} = D_{IS}^{(2)} = 1188$ Hz) under imperfect inhomogeneous HH matching ($\overline{\Delta} = \pm\,\omega_r$ and $\sigma_\Delta = 0.5$ kHz)

with an angle between the two I–S vectors $\chi = 90°$ (red line), $\chi = 71°$ or 109° (blue line), $\chi = 30°$ or 150° (green line), $\chi = 0$ or 180° (orange line). The CP signal amplitude under perfect homogeneous HH matching (case of the I–S spin pair) have been multiplied by a factor 0.57 for comparison of the time evolution.

Beside the above factors, the shortening of P–H distance to ca 3.4 Å, deduced directly from Fourier transform over the experimental CP MAS intensities (Fig. 7b) and by the model calculations (Fig. 8a, Table 1), can have an intriguing physical reason – proton conductivity. The crystalline CaHA is well-known as a proton conductor (see ref 8 and references cited therein). A large-amplitude motion of protons occurs along OH^- chains. It was succeeded to visualized the proton migration pathway through the neutron diffraction experiments.[7,8] It consists of the O–H tumbling and the short-range diffusion (Fig. 11). It is very likely that such zigzag motion causes the shortening of the effective P–H distance.

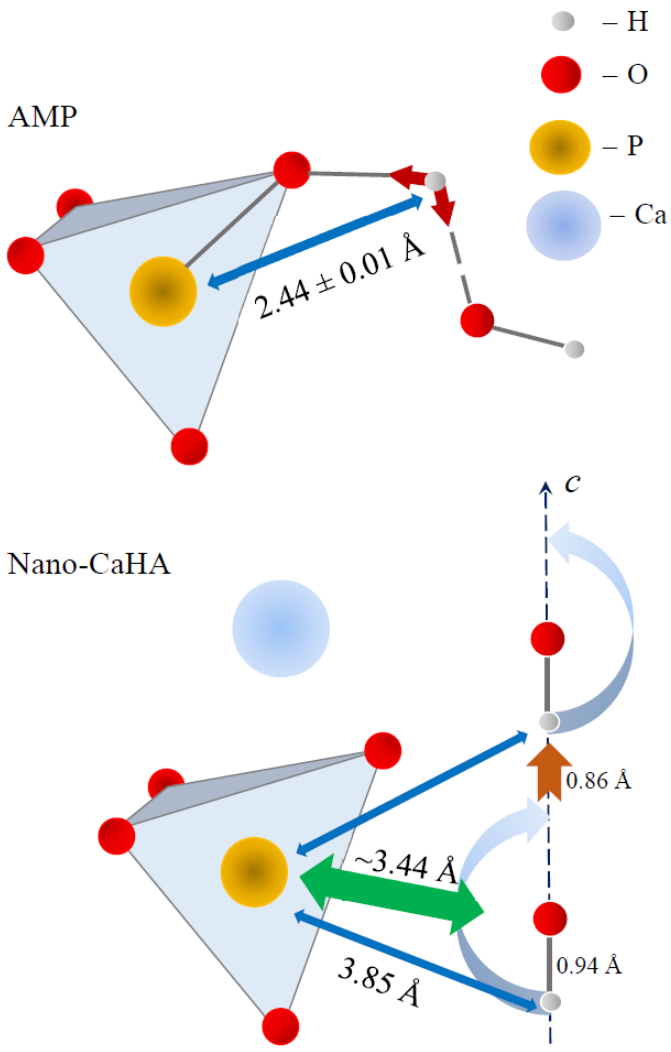

Fig. 11 The structural features of AMP and nano-CaHA. The proton migration pathway, the O–H bond length (0.94 Å) and the distance of short-range diffusion (0.86 Å) were taken from refs 7,8,26.

Conclusions

1. The combined analysis of the solid-state ^{1}H and ^{31}P NMR spectra provides the possibility to determine the hydration numbers of the components and the phase composition index.
2. The anisotropic spin dynamics models with the angular averaging of dipolar coupling were applied for amorphous CaP and nano-structured CaHA for the first time. It was deduced that the spin diffusion in AMP is close to isotropic ($R^{I}_{dp}/R^{\Sigma}_{df,} \approx 2$), whereas it is highly anisotropic in nano-CaHA being close to the Ising-type ($R^{I}_{dp}/R^{\Sigma}_{df} >> 1$). This can be caused by the different number of internuclear interactions that must be explicitly considered in the spin system for AMP (I–S spin pair) and nano-CaHA (I_N–S spin system with $N \geq 2$).
3. The spin-lattice relaxation in the rotating frame in AMP sample occurs in the time scale of $\sim 10^{-2}$ s as for ^{1}H as well as for ^{31}P spins. This process slowdowns with increasing amount of structural water (composite sample) and becomes infinitely slow in nano-CaHA.
4. The P–H distance in nano-CaHA was found being significantly shorter than its crystallographic value. This can be due to a certain overestimation of D_{IS} values caused by multiple-spin interactions and RF field mismatch/inhomogeneity, or alternatively - due to proton conductivity. In other words – in the systems with a large-amplitude proton motion the ^{1}H–^{31}P CP MAS kinetics provides a certain effective distance between ^{1}H and ^{31}P spins that can be shorter than the crystallographic, i.e. 'frozen', one.
5. The P–H distance deduced for AMP, i.e. the compound with HPO_4^{2-} as the dominant structure, is fairly well matching to the crystallographic data. If the formation of HPO_4^{2-} is considered as the proton transfer that goes via H-bonding PO_4^{3-}…H–O–H $\rightarrow$ HPO_4^{2-} + OH^{-}, the correct P–H distance is very promising result. This would mean that the CP MAS kinetics is a capable technique getting a complementary information on the proton localization in H-bond and the proton transfer in the cases, where traditional structure

determination methods do not work properly, e.g. soft disordered solids or gels, amorphous or nano-structured materials, supramolecular aggregates, etc.

Conflicts of interest

There are no conflicts to declare.

Acknowledgements

This research is funded by the European Social Fund under measure No 09.3.3-LMT-K-712-19-0022 “Development of Competences of Scientists, other Researchers and Students through Practical Research Activities” measure. The authors acknowledge the Center of Spectroscopic Characterization of Materials and Electronic/Molecular Processes ('Spectroversum', http://spectroversum.ff.vu.lt) for the use of spectroscopic equipment. Computations were performed on resources at the High Performance Computing Center of Vilnius University (´HPC Sauletekis´, http://supercomputing.ff.vu.lt).

References

1 W. Habraken, P. Habibovic, M. Epple and M. Bohner, *Materials Today,* 2016, **19**, 69-87.

2 P. W. Brown and B. Constantz, *Hydroxyapatite and Related Materials,* CRC Press, 1994.

3 R. Z. Le Geros and J. P. Le Geros, in: *Bioceramics and Their Clinical Applications,* ed. T. Kokubo, Woodhead Publishing, Cambridge, 2008.

4 A. Zanotto, M. L. Saladino, D. C. Martino and E. Caponetti, *Advances in Nanoparticles,* 2012, **1**, 21-28.

5 A. Kizalaite, I. Grigoraviciute-Puroniene, D. R. C. Asuigui, S. L. Stoll, S. H. Cho, T. Sekino, A. Kareiva and A. Zarkov, *ACS Biomater. Sci. Eng*., 2021, **7**, 3586-3593.

6 L. Sinusaite, I. Grigoraviciute-Puroniene, A. Popov, K. Ishikawa, A. Kareiva and A. Zarkov, *Ceram. Int.*, 2019, **45**, 12423-12428.

7 M. Yashima, N. Kubo, K. Omoto, H. Fujimori, K. Fujii and K. Ohoyama, *J. Phys. Chem. C,* 2014, **118**, 5180-5187.

8 M. Yashima, Y. Yonehara and H. Fujimori, *J. Phys. Chem. C,* 2011, **115**, 25077-25087.

9 M. Ben Osman, S. Diallo-Garcia, V. Herledan, D. Brouri, T. Yoshioka, J. Kubo, Y. Millot and G. Costentin, *J. Phys. Chem. C,* 2015, **119**, 23008-23020.

10 J. Kolmas, A. Jaklewicz, A. Zima, M. Bućko, Z. Paszkiewicz, J. Lis, A. Ślosarczyk and W. Kolodziejski, *J. Mol. Struct*., 2011, **987**, 40-50.

11 R. Mathew, P. N. Gunawidjaja, I. Izquierdo-Barba, K. Jansson, A. Garcia, D. Arcos, M. Vallet-Regi and M. Eden, *J. Phys. Chem. C,* 2011, **115**, 20572-20582.

12 A. Vyalikh, P. Simon, E. Rosseeva, J. Buder, R. Kniep and U. Scheler, *J. Phys. Chem. B,* 2014, **118**, 724-730.

13 C. Jäger, T. Welzel, W. Meyer-Zaika and M. Epple, *Magn. Reson. Chem.,* 2006, **44**, 573-580.

14 E. E. Wilson, A. Awonusi, M. D. Morris, D. H. Kohn, M. M. J. Tecklenburg and L. W. Beck, *Biophys. J.,* 2006, **90**, 3722-3731.

15 E. Davies, M. J. Duer, S. E. Ashbrook and J. M. Griffin, *J. Am. Chem. Soc.,* 2012, **134**, 12508-12515.

15 E. O. Stejskal, J. Schaefer and J. S. Waugh, *J. Magn. Reson*., 1977, **28**, 105−112.

16 M. H. Levitt, D. Suter and R. R. Ernst, *J. Chem. Phys*., 1986, **84**, 4243-4255.

17 S. V. Dvinskikh, H. Zimmermann, A. Maliniak and D. Sandström, *J. Chem. Phys*., 2005, **122**, 044512(12).

18 J. Raya and J. Hirschinger, *J. Magn. Reson*., 2017, **281**, 253-271.

19 W. Kolodziejski and J. Klinowski, *Chem. Rev*., 2002, **102**, 613-628.

20 L. Dagys, V. Klimavicius, T. Gutmann, G. Buntkowsky and V. Balevicius, *J. Phys. Chem. A,* 2018**, 122**, 8938-8947.

21 P. Bertani, J. Raya, P. Reinheimer, R. Gougeon, L. Delmotte and J. Hirschinger, *Solid State Nucl. Magn. Reson.,* 1999, **13**, 219-229.

22 J. Raya, A. Bianco and J. Hirschinger, *Phys. Chem. Chem. Phys*., 2020, **22**, 12209-12227.

23 V. Klimavicius, L. Dagys and V. Balevicius, *J. Phys. Chem. C,* 2016, **120**, 3542-3549.

24 V. Klimavicius, A. Kareiva and V. Balevicius, *J. Phys. Chem. C,* 2014, **118**, 28914-28921.

25 A. Kaflak-Hachulska, A. Samoson and W. Kolodziejski, *Calcif. Tissue Int*., 2003, **73**, 476-486.

26 W. Kolodziejski, *Top. Curr. Chem*., 2004, **246**, 235-270.

27 K. Sudarsanan and R. A. Young, *Acta Crystallogr. B,* 1969, **25**, 1534-1543.

28 C. Adamo and V. Barone, *J. Chem. Phys.,* 1999, **110**, 6158-6170.

29 M. J. Frisch, G. W. Trucks, H. B. Schlegel, G. E. Scuseria, M. A. Robb, J. R. Cheeseman, G. Scalmani, V. Barone, G. A. Petersson, H. Nakatsuji, X. Li, M. Caricato, A. V. Marenich, J. Bloino, B. G. Janesko, R. Gomperts, B. Mennucci, H. P. Hratchian, J. V. Ortiz, A. F. Izmaylov, J. L. Sonnenberg, D. Williams-Young, F. Ding, F. Lipparini, F. Egidi, J. Goings, B. Peng, A. Petrone, T. Henderson, D. Ranasinghe, V. G. Zakrzewski, J. Gao, N. Rega, G. Zheng, W. Liang, M. Hada, M. Ehara, K. Toyota, R. Fukuda, J. Hasegawa, M. Ishida, T. Nakajima, Y. Honda, O. Kitao, H. Nakai, T. Vreven, K. Throssell, J. A. Montgomery, Jr., J. E. Peralta, F. Ogliaro, M. J. Bearpark, J. J. Heyd, E. N. Brothers, K. N. Kudin, V. N. Staroverov, T. A. Keith, R. Kobayashi, J. Normand, K. Raghavachari, A. P. Rendell, J. C. Burant, S. S. Iyengar, J. Tomasi, M. Cossi, J. M. Millam, M. Klene, C. Adamo, R. Cammi, J. W. Ochterski, R. L. Martin, K. Morokuma, O. Farkas, J. B. Foresman and D. J. Fox, *Gaussian 16, Revision C.01,* Gaussian, Inc., Wallingford CT, 2016.

30 V. Balevicius, Z. Gdaniec and K. Aidas, *Phys. Chem. Chem. Phys.,* 2009, **11**, 8592-8600.

31 L. Müller, A. Kumar, T. Baumann and R. R. Ernst, *Phys. Rev. Lett*., 1974, **32**, 1402-1406.

32 J. Hirschinger and J. Raya, *Mol. Phys*., 2015, **113**, 3161-3175.

33 C. A. Fyfe, A. R. Lewis and J. M. Chézeau, *Can. J. Chem*., **1999**, *77*, 1984-1993.

34 L. Dagys, V. Klimavicius and V. Balevicius, *J. Chem. Phys.,* 2016, **145**, 114202 (9).

35 A. Naito and C. A. McDowell, *J. Chem. Phys*., 1986, **84**, 4181-4186.

36 J. Hirschinger and J. Raya, *to be published*.

37 V. Klimavicius, L. Dagys, V. Chizhik and V. Balevicius, *Appl. Magn. Reson.,* 2017, **48**, 673-685.

38 V. Balevicius and K. Aidas, *Appl. Magn. Reson.,* 2007, **32**, 363-376.

39 V. Balevicius, V. J. Balevicius, K. Aidas and H. Fuess, *J. Phys. Chem. B,* 2007, **111**, 2523-2532.

40 V. Klimavicius, L. Dagys, V. Klimkevičius, D. Lengvinaitė, K. Aidas, S. Balčiūnas, J. Banys, V. Chizhik and V. Balevicius, *J. Phys. Chem. B,* 2021, **125**, 12592-12602.

41 V. Klimavicius, F. Kuliešius, E. Orentas and V. Balevicius, *Lith. J. Phys.,* 2021, **61**, 27-34.

42 R. Gupta, G. Hou, T. Polenova and A. J. Vega, *Solid State Nucl. Magn. Reson.,* 2015, **72**, 17-26.

43 B. B. Kharkov, V. I. Chizhik and S. V. Dvinskikh, *J. Chem. Phys*., 2016, **144**, 034201(10).

44 M. Hologne, P. Bertani, T. Azraïs, C. Bonhomme and J. Hirschinger, *Solid State Nucl. Magn. Reson.,* **2005**, **28**, 50-56.

45 A. K. Chattah, G. A. Alvarez, P. R. Levstein, F. M. Cucchietti, H. M. Pastawski, J. Raya and J. Hirschinger, *J. Chem. Phys*., 2003, **119**, 7943-7951.

46 J. Brus and J. Jakes, *Solid State Nucl. Magn. Reson.,* 2005, **27**, 180-191.

47 P. Paluch, J. Trébosc, Y. Nishiyama, M. J. Potrzebowski, M. Malon and J. P. Amoureux, *J. Magn. Reson*., 2015, **252**, 67-77.

48 P. Paluch, T. Pawlak, J. P. Amoureux and M. J. Potrzebowski, *J. Magn. Reson*., 2013, **233**, 56-63.

49 S. Hediger, B. H. Meier and R. R. Ernst, *Chem. Phys. Lett*., 1993, **213**, 627-635.

50 A. C. Kolbert and S. L. Gann, *Chem. Phys. Lett*., 1994, **224**, 86-90.

51 R. Zhang, J. Damron, T. Vosegaard and A. Ramamoorthy, *J. Magn. Reson.,* 2015, **250**, 37-44.

Table of contents

Structural and dynamical evolution in series amorphous phosphate - composite - nano-structured calcium hydroxyapatite is probed by NMR cross-polarization kinetics

Graphical Abstract